arXiv:2601.17354v2 [cs.CV] 28 Jan 2026

PocketGS: On-Device Training of 3D Gaussian Splatting for High Perceptual Modeling

Wenzhi Guo, Guangchi Fang, Shu Yang, Bing Wang*

Fig. 1: Our PocketGS enables high-quality end-to-end 3DGS reconstruction on commodity smartphones. Compared to standard 3DGS workstation baselines, PocketGS achieves superior visual fidelity (LPIPS: 0.108) within a tight training budget (500 iterations, ∼4 minutes on an iPhone 15).

***Abstract*—Efficient and high-fidelity 3D scene modeling is a long-standing pursuit in computer graphics. While recent 3D Gaussian Splatting (3DGS) methods achieve impressive real-time modeling performance, they rely on resource-unconstrained training assumptions that fail on mobile devices, which are limited by minute-scale training budgets and hardware-available peak-memory. We present PocketGS, a mobile scene modeling paradigm that enables on-device 3DGS training under these tightly coupled constraints while preserving high perceptual fidelity. Our method resolves the fundamental contradictions of standard 3DGS through three co-designed operators: $\mathcal{G}$ builds geometry-faithful point-cloud priors; $\mathcal{I}$ injects local surface statistics to seed anisotropic Gaussians, thereby reducing early conditioning gaps; and $\mathcal{T}$ unrolls alpha compositing with cached intermediates and index-mapped gradient scattering for stable mobile backpropagation. Collectively, these operators satisfy the competing requirements of training efficiency, memory compactness, and modeling fidelity. Extensive experiments demonstrate that PocketGS is able to outperform the powerful mainstream workstation 3DGS baseline to deliver high-quality reconstructions, enabling a fully on-device, practical capture-to-rendering workflow.**

***Index Terms*—3D Gaussian Splatting, Rendering, on-devide, modeling system.**

I. Introduction

3D Gaussian Splatting (3DGS) [1] is a promising paradigm for high-quality scene modeling, advancing mixed reality [2], [3], digital twins [4], [5], and robotic simulation [6], [7]. By replacing implicit neural representations [8] with rasterization-friendly 3D Gaussians, it achieves real-time high-fidelity modeling, but still suffers from high computation, memory overhead, and training time, hindering on-device training for mobile 3D content creation.

Training 3DGS on device introduces substantial challenges, as it must deliver high perceptual quality under the limited computational resources and strict thermal constraints of mobile platforms. Consequently, the training process must meet **on-device constraints**: 1) completion within a few minutes ($<$5 min), 2) respecting the hardware-available memory budget ($<$3 GB).

These constraints require rethinking 3DGS under resource-limited regimes beyond conventional resource-unconstrained assumptions. Gaussian-based modeling typically includes: (1) recovering camera parameters and a point cloud from images, (2) initializing 3D Gaussians from this geometry, and (3) optimizing the Gaussians via differentiable rendering for scene recovery.

Existing designs assume ample time and memory across all stages, but on-device settings break these assumptions, yielding three tightly coupled contradictions.

Input-Recovery Contradiction. A primary limitation of on-device 3DGS arises from the contradiction between unreliable geometric input and accurate scene recovery. Mobile scans provide coarse geometry as imprecise poses and sparse points, causing noisy initialization. Existing methods compensate by densifying Gaussians, but this raises computation and memory overhead, leading to long training times and

memory overflow. *Consequently, on-device 3DGS requires reliable geometric input to minimize reliance on excessive densification for scene recovery.*

Initialization-Convergence Contradiction. Another key limitation lies in the contradiction between heuristic initialization and stable convergence. Existing methods disregard geometric priors and initialize input points as isotropic 3D Gaussians, relying on prolonged optimization to compensate for the resulting deficiencies. Under on-device constraints, extra iterations are costly and violate time, energy, and thermal budgets. *Thus, on-device 3DGS requires geometry-conditioned initialization to reduce optimization burden, thereby facilitating stable convergence.*

Hardware-Differentiability Contradiction. On-device 3DGS is at odds with mobile execution: differentiable rendering requires storing intermediates for backpropagation, but mobile pipelines restrict gradient access through opaque blending, suffer from costly GPU–CPU synchronization in optimization, and incur heavy data movement and state misalignment from depth-ordered alpha blending. *Therefore, on-device 3DGS requires a mobile-oriented differentiable rendering framework that bounds and replays only the necessary intermediates for Gaussian optimization.*

In this work, we present **PocketGS**, a 3DGS training paradigm that achieves high-perceptual modeling under on-device constraints via three co-designed operators (Fig. **??**,2). To address the Input-Recovery Contradiction, the geometry-prior construction operator $\mathcal{G}$ builds a geometry-faithful prior, providing the required geometric guidance without costly in-loop Gaussian densification beyond the on-device envelope. To resolve the Initialization-Convergence Contradiction, the prior-conditioned Gaussian parameterization operator $\mathcal{I}$ uses this prior to shape initial Gaussians, improving conditioning for stable, iteration-limited optimization and reducing degradation from noise-sensitive initialization. Finally, to overcome the Hardware-Differentiability Contradiction, the hardware-aligned splatting optimization operator $\mathcal{T}$ makes differentiable rendering practical on mobile GPUs, preserving correct gradients and stable updates without prohibitive memory traffic or CPU–GPU synchronization. Extensive experiments show that PocketGS achieves perceptual quality superior to mainstream workstation 3DGS baselines, while operating within on-device constraints.

Our main contributions are:

- We introduce a geometry-prior construction operator $\mathcal{G}$ that provides compact yet reliable geometric inputs for on-device 3DGS, reducing the dependence on heavy-weight reconstruction and costly training-time densification.
- We propose a prior-conditioned Gaussian parameterization operator $\mathcal{I}$ that improves initialization quality and optimization conditioning, enabling stable convergence under a strict on-device iteration budget.
- We develop a hardware-aligned splatting optimization operator $\mathcal{T}$ that renders differentiable splatting practical on mobile GPUs, supporting accurate gradients and stable updates within hardware memory and bandwidth constraints.
- We validate that, while satisfying on-device constraints, PocketGS achieves competitive perceptual quality relative to standard workstation 3DGS pipelines on publicly available benchmarks and our self-collected MobileScan datasets.

II. Related Work

A. Novel View Synthesis

Novel view synthesis targets photorealistic rendering from unseen viewpoints [9], [10]. The field has progressed from implicit NeRF-style radiance fields [8], [11], [12] to more efficient explicit voxel/hash-grid representations [13]–[17], and further to 3DGS with rasterization-friendly Gaussians for fast training and rendering [1], [18], [19]. Despite advances [4], [20]–[26], most 3DGS pipelines still rely on offline SfM [27], [28] for pose and sparse geometry, whose high cost and incomplete coverage hinder practical on-device training in resource-constrained settings.

B. Mobile 3D Scanning

Mobile 3D scanning captures images on mobile devices and reconstructs real-world 3D structure, typically via visual-inertial odometry for pose estimation and multi-view stereo for geometry [29]–[32]. Systems such as ARKit and ARCore follow this pipeline [33]–[35] but are limited by point/mesh representations, whose sparse and noisy reconstructions lack the capacity for high-fidelity rendering [9], [10]. Meanwhile, novel view synthesis has shown superior modeling and rendering quality, opening new opportunities for mobile 3D scanning [1], [9]; however, existing efforts largely emphasize mobile rendering efficiency [36], [37], leaving on-device training underexplored.

III. The PocketGS Paradigm

PocketGS enables on-device 3DGS training: given a short mobile capture I_t, it optimizes a Gaussian scene Θ under strict runtime and peak-memory budgets on tile-based mobile GPUs. It co-designs three coupled operators: $\mathcal{G}$ derives a compact geometry prior $\mathcal{P}$ from I_t, $\mathcal{I}$ uses $\mathcal{P}$ to initialize well-conditioned Gaussians Θ_0, and $\mathcal{T}$ performs hardware-aligned differentiable splatting to keep training GPU-resident with correct gradients. Formally, $\mathcal{G} : (\{I_t\}, \{\hat{T}_t\}) \mapsto (\{T_t\}, \mathcal{P})$, $\mathcal{I} : \mathcal{P} \mapsto \Theta_0$, and $\mathcal{T} : (\Theta_0, \{I_t, T_t\}) \mapsto \Theta^*$, balancing perceptual quality with on-device constraints.

A. Geometry Prior Construction under Resource Budgets

To resolve the Input-Recovery Contradiction, Operator $\mathcal{G}$ constructs a low-noise and low-redundant 3DGS-aligned prior within mobile compute and memory constraints. Treating BA (Bundle Adjustment) and MVS (Multi-View Stereo) as core prior-construction primitives, their outputs directly condition the 3DGS optimization, mitigating over-reliance on excessive in-loop Gaussian densification.

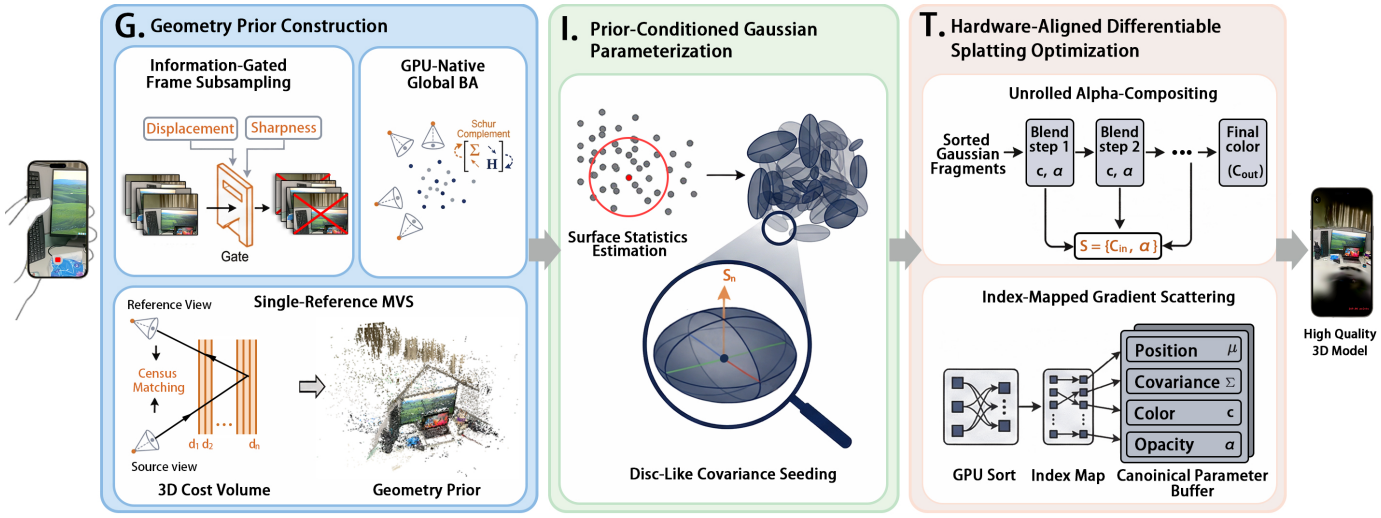

Fig. 2: **Overview of the PocketGS framework.** PocketGS tackles on-device 3DGS training through three coupled operators: ($\mathcal{G}$) Geometry Prior Construction employs an information-gated gate for frame selection, followed by GPU-native Schur-complement BA and single-reference MVS. The MVS module constructs a 3D cost volume by sampling depth hypotheses $d_1, \ldots, d_n$ via census matching to produce a dense geometric scaffold. ($\mathcal{I}$) Prior-Conditioned Parameterization seeds anisotropic Gaussians by estimating local surface statistics (normals $\mathbf{s}_n$ and scales) to front-load structure discovery via disc-like covariance seeding. ($\mathcal{T}$) Hardware-Aligned Splatting implements a mobile-native differentiable renderer using unrolled alpha-compositing ($S = C_{in}, \alpha$) and index-mapped gradient scattering to ensure stable backpropagation within tight mobile memory bounds of the canonical parameter buffer (μ, Σ, c, α).

1) Information-Gated Frame Subsampling: To reduce input noise and provide high-quality photometric ground truth for 3DGS training, PocketGS adopts a real-time three-stage gating mechanism that admits only frames with incremental geometric utility, maximizing information yield per compute unit.

Displacement Gate. We ensure sufficient parallax for robust triangulation by computing the camera displacement d between the current frame and the last selected keyframe, $d = \|\mathbf{t}_{curr} - \mathbf{t}_{last}\|_2$. A frame is considered only if $d \geq \tau_d$, where $\tau_d = 0.05m$, suppressing redundant viewpoints while maintaining tracking stability.

Sharpness Heuristic. We reject frames degraded by motion or defocus blur using an efficient approximation of gradient energy. We estimate the sharpness score S by summing absolute luma differences over a sparsely sampled grid Ω:

$$S = \frac{1}{|\Omega|} \sum_{(x,y)\in\Omega} \left(|I(x+\Delta, y) - I(x,y)| + |I(x, y+\Delta) - I(x,y)|\right) \tag{1}$$

where Δ is the step size. This score correlates with high-frequency content and favors sharp frames.

Candidate Windowing. We select the locally optimal frame from a short temporal window (8 frames or 250ms). A candidate replaces the current best only if $S_{new} > (1+r)S_{best}$, with $r = 0.05$. This commits the sharpest representative per viewpoint and bounds downstream optimization workload.

Keyframe admission is explicitly bounded by the three gates, reducing downstream BA/MVS workload roughly proportional to admitted keyframes rather than raw capture length, thereby constraining both runtime and peak intermediate storage.

2) GPU-Native Global BA as Mobile MAP Refinement: To address mobile input imprecision, PocketGS implements GPU-native global BA to jointly optimize poses and 3D points, delivering 3DGS-required precision without over-densification. The robustified reprojection objective for PocketGS:

$$\min_{\{\mathbf{T}_i\},\{\mathbf{P}_j\}} \sum_{i,j} \rho\left(\|\pi(\mathbf{T}_i, \mathbf{P}_j) - \mathbf{p}_{ij}\|^2_{\Sigma_{ij}}\right) \tag{2}$$

where π is the projection function, $\mathbf{T}_i \in SE(3)$ is the pose of camera i, $\mathbf{P}_j \in \mathbb{R}^3$ is the 3D position of point j, $\mathbf{p}_{ij} \in \mathbb{R}^2$ is the observed 2D projection, and ρ is the robust Huber loss.

Scale-Aware Gauge Fixing. To resolve the 7-DoF ambiguity of monocular reconstruction, we fix the 6-DoF pose of the first keyframe and fix scale by constraining the translational component of the second keyframe along the dominant baseline axis, yielding a consistent metric frame.

GPU-Native Schur Complement. The BA bottleneck is solving the normal equations $\mathbf{H}\Delta = \mathbf{b}$, where $\mathbf{H} = \mathbf{J}^T\mathbf{J}$. We exploit the sparse block structure via a full GPU Schur complement. Partitioning parameters into camera pose (c) and point (p) blocks yields the reduced camera system:

$$(\mathbf{H}_{cc} - \mathbf{H}_{cp}\mathbf{H}_{pp}^{-1}\mathbf{H}_{pc})\Delta_c = \mathbf{b}_c - \mathbf{H}_{cp}\mathbf{H}_{pp}^{-1}\mathbf{b}_p \tag{3}$$

Since $\mathbf{H}_{pp}$ is block-diagonal with independent 3×3 blocks per point, $\mathbf{H}_{pp}^{-1}$ is computed in parallel across points on the GPU. After solving for Δ_c, we recover Δ_p by back-substitution.

Iterative Geometric Refinement. BA is embedded in an iterative refinement loop. After each global step, we re-triangulate features using updated poses, filter points with high reprojection error or insufficient triangulation angles, and remove observations behind the camera. This purification reduces outliers and stabilizes dense reconstruction.

Schur complement reduces solving from the full joint system to a smaller camera system, while $\mathbf{H}_{pp}^{-1}$ is computed in parallel; the design keeps memory dominated by sparse observations rather than dense matrices, making global refinement feasible on-device.

3) Single-Reference Cost-Volume MVS: To address mobile input sparsity, PocketGS's lightweight MVS generates a dense geometry-faithful point cloud, providing structural richness for Gaussian initialization without over-densification.

Probabilistic Depth Range Estimation. Plane-sweep efficiency depends on depth range. For each target frame, we project sparse BA points and compute the 5% and 95% depth quantiles $q_{.05}$ and $q_{.95}$. We define the search range as $[q_{.05} \cdot 0.6, q_{.95} \cdot 1.6]$, focusing computation on the most probable volume.

Memory-Efficient Cost Volume. To minimize memory footprint, we construct the cost volume using only a single, optimally chosen reference frame. The reference maximizes

$$S_{ref} = \exp\left(-\frac{(b - b_{target})^2}{2\sigma_b^2}\right) \cdot \max\left(\frac{\alpha}{\alpha_{min}}, 1\right) \tag{4}$$

balancing baseline length b against a target baseline b_{target} and enforcing sufficient viewing angle α. The matching cost is computed using the Census Transform [38] for robustness to illumination changes. Depth is inferred via plane sweep [39] with Semi-Global Matching aggregation. We filter depth maps using a confidence threshold of 0.4 and fuse them into a dense point cloud, which serves as the geometric scaffold for $\mathcal{I}$.

B. Prior-Conditioned Gaussian Parameterization

To ensure stable convergence under a strict mobile iteration budget, operator $\mathcal{I}$ improves early-stage conditioning by replacing isotropic initialization with prior-conditioned, surface-aligned anisotropic Gaussians, thereby injecting structural cues from $\mathcal{G}$ and reducing reliance on photometric signals to infer geometry.

1) Local Surface Statistics Estimation: To inject geometric prior knowledge into initialization, we estimate local surface statistics for each point $\mathbf{p}_i$ in the dense MVS point cloud via KNN (K=16). The neighborhood covariance matrix is computed as:

$$\mathbf{C} = \frac{1}{K}\sum_{k=1}^{K}(\mathbf{p}_k - \bar{\mathbf{p}})(\mathbf{p}_k - \bar{\mathbf{p}})^T \tag{5}$$

where $\bar{\mathbf{p}}_i$ is the centroid of the neighborhood.The eigenvector corresponding to $\mathbf{C}_i$'s smallest eigenvalue robustly estimates the local surface normal $\mathbf{n}_i$. This GPU-parallelized process provides critical structural cues for informed initialization.

Fixed local neighborhood size ensures embarrassingly parallel computation with bounded per-point memory, aligning with PocketGS's mobile constraints.

2) Disc-Like Covariance Seeding: We initialize each Gaussian as a thin, disc-like ellipsoid tangent to the estimated surface, directly addressing the contradiction by replacing naive isotropic initialization with geometry-conditioned anisotropy. The tangential scale s_t is derived from local point density, estimated as the average distance to the K=3 nearest neighbors:

$$s_t = \frac{1}{3}\sum_{k=1}^{3}\|\mathbf{p} - \mathbf{p}_k\| \tag{6}$$

We set the normal-direction scale s_n as a fraction of tangential scale:

$$s_n = s_t \times r_{normal} \tag{7}$$

where $r_{normal} = 0.3$. Scale parameters are optimized in log-space, $\mathbf{s}_{log} = \log(\mathbf{s})$, ensuring positivity and numerical stability. The initial rotation $\mathbf{q}$ aligns the Gaussian local z-axis with the estimated surface normal $\mathbf{n}_i$. Opacity is initialized to a fixed low value (logit of 0.1). This geometry-conditioned anisotropy supplies strong priors on surface orientation and extent, accelerating convergence under limited iterations.

C. Hardware-Aligned Differentiable Splatting Optimization

Operator $\mathcal{T}$ rewrites the 3DGS training loop for GPU-resident optimization on mobile GPUs under tight memory/bandwidth budgets, reducing intermediate storage and synchronization overhead while enabling differentiable blending. By unrolling compositing and decoupling parameter/state layout from rendering order, it supports end-to-end on-device training with correct, stable gradients.

1) Unrolled Alpha-Compositing with Forward Replay Cache: To address hidden intermediate states, PocketGS unrolls alpha-compositing into an explicit differentiable pipeline with cached intermediates. Standard front-to-back compositing follows:

$$C_{out} = C_{in}(1 - \alpha) + \alpha c, \tag{8}$$

where C_{in} is the pre-composite color, and (α, c) are the opacity and color of the current Gaussian fragment. In a mobile rendering pipeline, hardware blending returns only C_{out} while hiding intermediate factors, making correct gradient propagation unavailable without costly framebuffer reads.

a) Explicit Computation Graph.: We process visible Gaussians in depth-sorted batches. Each batch explicitly takes the previous accumulator as input, exposing the intermediates necessary for the backward pass:

$$\frac{\partial \mathcal{L}}{\partial C_{in}} = \frac{\partial \mathcal{L}}{\partial C_{out}}(1 - \alpha), \quad \frac{\partial \mathcal{L}}{\partial \alpha} = \frac{\partial \mathcal{L}}{\partial C_{out}}(c - C_{in}). \tag{9}$$

b) Bandwidth-Efficient Cache.: To minimize memory bandwidth pressure-a critical constraint for mobile energy efficiency-we introduce a forward replay cache. Instead of caching full per-pixel splat lists, we store a minimal set $S = \{C_{in}, \alpha\}$ and use a per-pixel counter buffer. By resetting only the $O(WH)$ counter rather than the entire $O(WHK_{max})$ cache, we significantly reduce the bandwidth overhead during the backward traversal.

2) Index-Mapped Gradient Scattering: Maintaining optimizer consistency during depth-sorted rendering typically requires physical memory reordering, which incurs heavy data movement. We resolve this by decoupling the *sorted view* from the *canonical layout*. A GPU-based sort generates an index list π, allowing the renderer to access parameters $\theta_{\pi(i)}$ while

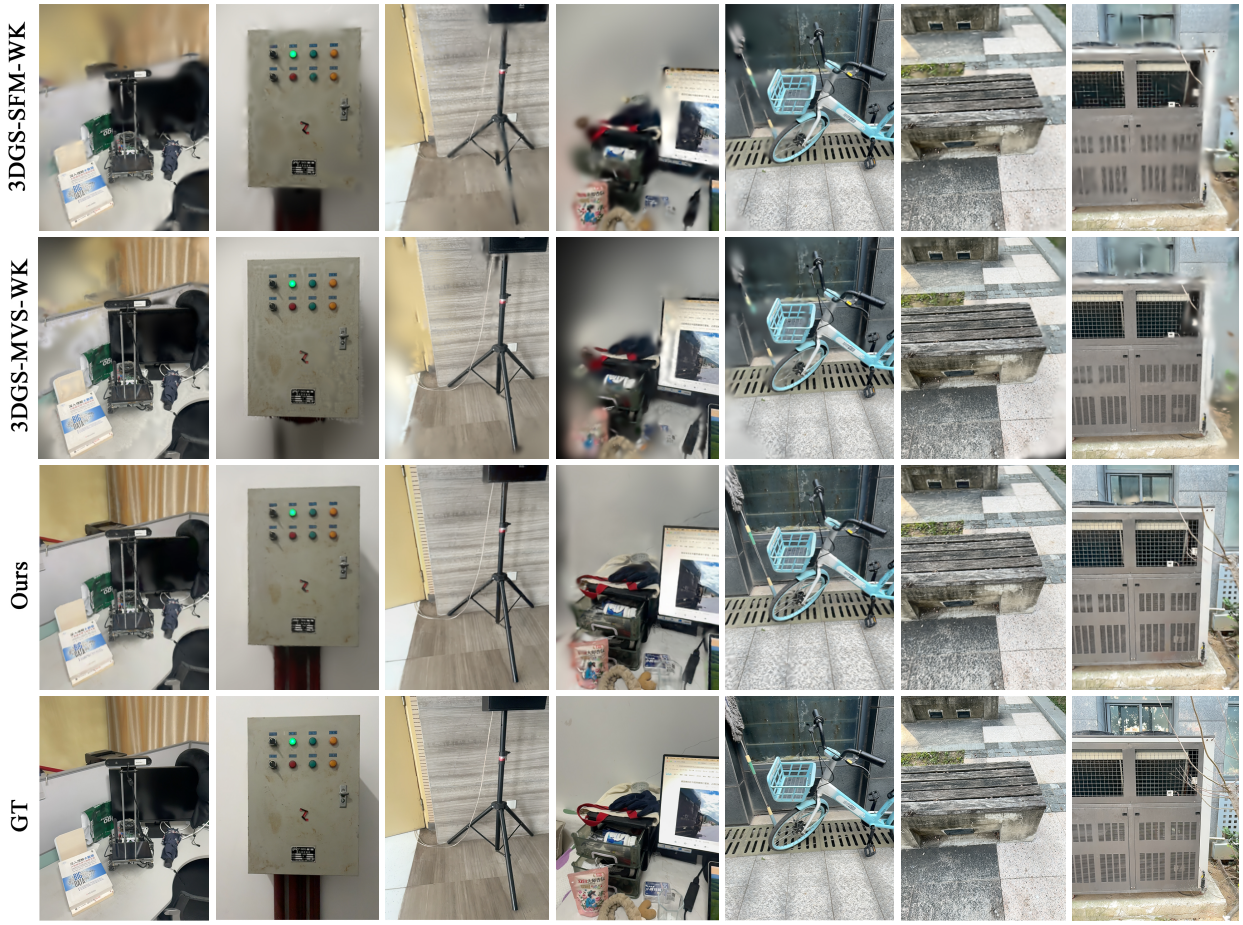

Fig. 3: Qualitative comparison on our MobileScan dataset. PocketGS (Ours) consistently recovers sharper textures and finer details compared to baselines. Notably, 3DGS-MVS-WK suffers from artifacts despite its high-density prior, as the over-concentrated initial points impede effective Gaussian redistribution within a limited iteration budget. Our method avoids this bottleneck through prior-conditioned initialization, achieving superior structural fidelity (e.g., bicycle spokes) that closely matches the ground truth (GT).

they remain stationary in memory. During backpropagation, gradients are scattered back to the canonical buffers:

$$\nabla\theta_{\pi(i)} += g_i, \tag{10}$$

ensuring that Adam optimizer states remain aligned with their respective parameters without CPU intervention or redundant memory copies.

3) On-GPU Parameter Optimization: To eliminate the synchronization latency of CPU-driven updates, the entire optimization loop is executed on-device. We maintain Adam states (moments m, v) in dedicated GPU buffers and perform updates via a unified compute kernel. To ensure convergence under limited FP16 precision, we employ specialized parameterization: **Opacity** uses logit-space updates with a micro-step threshold; **Scale** is optimized in log-space with explicit clamping; and **Rotation** is updated via tangent-space projection and sign-unification. This fully GPU-resident schedule minimizes the host-device communication footprint while maximizing hardware utilization.

IV. Experiments

A. Experimental Setup

1) Implementation Details and Experimental Settings: We implement PocketGS as a fully on-device system and evaluate it on an iPhone 15 (Apple A16). The entire process was written in Swift and accelerated by using the Apple Metal API to take advantage of the mobile GPU execution stack. Unless otherwise stated, all methods are evaluated under identical image resolution, color space, and metric implementations.

To reflect realistic mobile constraints, we use a fixed training budget for all methods. In particular, we optimize each model for a constant number of iterations (500 iterations) at a fixed view rendering resolution.

2) Baselines: We compare against two workstation baselines that follow the standard two-stage paradigm: (i) reconstruct camera poses and a point-cloud prior, and (ii) train a standard 3D Gaussian Splatting (3DGS) model initialized from the reconstructed prior. All workstation experiments are conducted on a machine equipped with 2× NVIDIA RTX 3090 GPUs and an Intel Core i9-class CPU. For both baselines, point-cloud reconstruction is performed using COLMAP [28].

Method	LLFF					NeRF-Synthetic					MobileScan				
	PSNR↑	SSIM↑	LPIPS↓	Time↓(s)	Count	PSNR↑	SSIM↑	LPIPS↓	Time↓(s)	Count	PSNR↑	SSIM↑	LPIPS↓	Time↓(s)	Count
3DGS-SFM-WK	21.01	0.641	0.405	108.0	18k	21.75	0.800	0.243	**83.7**	12k	21.16	0.687	0.398	**112.8**	23k
3DGS-MVS-WK	19.53	0.637	0.387	313.1	40k	**24.47**	**0.887**	**0.128**	532.1	50k	20.85	0.781	0.281	534.5	165k
PocketGS (Ours)	**23.54**	**0.791**	**0.222**	**105.4**	33k	24.32	0.858	0.144	101.4	47k	**23.67**	**0.791**	**0.225**	255.2	168k

TABLE I: **Average Metrics Across Datasets.** Dataset-level averages on LLFF, NeRF Synthetic, and our MobileScan mobile-native dataset. Higher is better for PSNR/SSIM, and lower is better for LPIPS/Time. Best results are in **bold**.

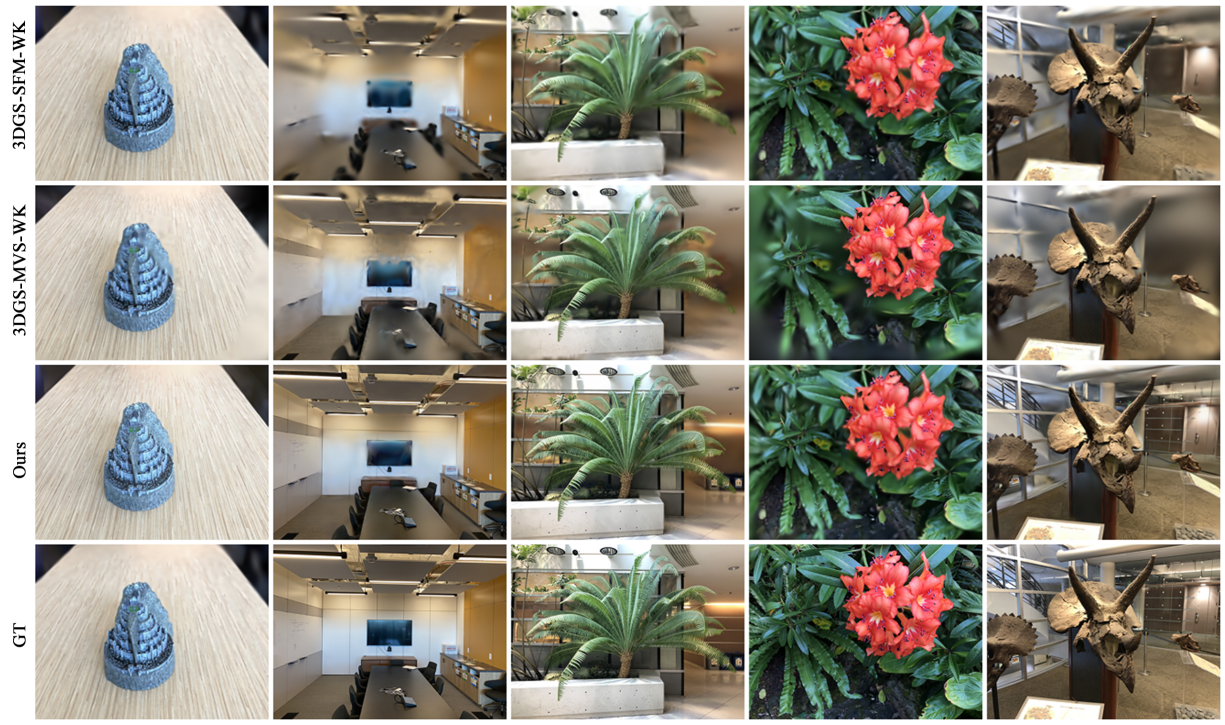

Fig. 4: **Qualitative comparison on the LLFF dataset.** Our method produces much sharper textures and more accurate thin structures (e.g., the leaves in Fern and the petals in Flower), closely matching the ground truth (GT).

a) 3DGS-SFM-WK: We adopt the standard COLMAP-based Structure-from-Motion (SfM) pipeline on a workstation to estimate camera extrinsic/intrinsic parameters and reconstruct a sparse point cloud. This sparse geometric prior is then used to initialize and train a vanilla 3D Gaussian Splatting (3DGS) model, adhering to the original 3DGS training protocol.

b) 3DGS-MVS-WK: For this workstation-based baseline, we leverage the standard COLMAP Multi-View Stereo (MVS) workflow to generate a dense point cloud as the geometric prior. Subsequently, a vanilla 3DGS model is initialized with this dense point cloud and trained following the default 3DGS optimization workflow.

We choose these two baselines because they (1) represent the standard reconstruction-first 3DGS pipeline, (2) span sparse SfM versus dense but costly MVS priors to separate prior quality from reconstruction overhead under matched budgets, and (3) provide a workstation reference that reflects PocketGS's goal: competitive quality under strict on-device constraints without heavy offline reconstruction.

3) Datasets and Metrics:

a) Datasets.: We evaluate on three representative datasets spanning synthetic and real captures: NeRF-Synthetic [8], LLFF [40], and MobileScan. NeRF-Synthetic provides object-centric synthetic scenes with accurate poses; LLFF consists of real forward-facing captures exhibiting real-world degradations; and MobileScan is our Phone-captured dataset designed to reflect mobile imaging characteristics, including motion blur, defocus, and exposure variation. For MobileScan, we use ARKit-provided intrinsics, poses, and sparse structure to emulate practical on-device inputs, enabling evaluation under noisy geometric priors and limited compute budgets. More details are in the supplement.

b) Metrics.: We report standard novel-view synthesis metrics, including PSNR (dB, ↑), SSIM (↑), and LPIPS (↓). We additionally report end-to-end runtime to capture practical deployability. Specifically, we define the total runtime as

$$T_{\text{total}} = T_{\text{geom}} + T_{\text{train}}, \tag{11}$$

where T_{geom} includes geometry and pose acquisition as well as associated optimization, and T_{train} denotes the 3DGS optimization time. For fair comparison, all methods are evaluated under the same training budget and at the same rendering

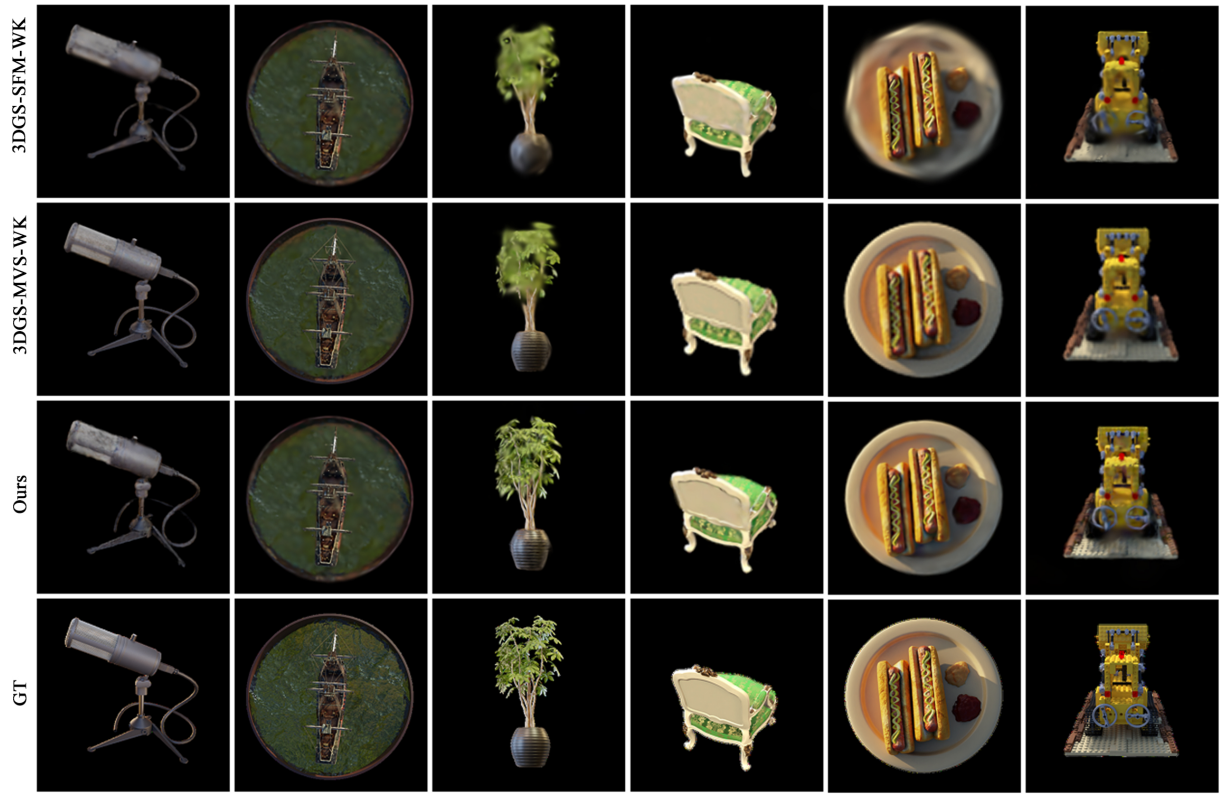

Fig. 5: **Qualitative comparison on the NeRF Synthetic dataset.** In these object-centric synthetic scenes, our method produces high-fidelity results.

resolution. Finally, we report Count (the number of Gaussians) to characterize the trade-off between representation capacity and computational efficiency.

B. Main Results: Quality and Efficiency Comparison

Table I summarizes averages under a strict, matched optimization budget. Across all datasets, PocketGS consistently delivers a strong quality–efficiency trade-off while maintaining *compact or comparable* Gaussian counts, indicating better representation efficiency.

a) LLFF Dataset.: LLFF stresses forward-facing captures and view extrapolation, where imperfect geometry can destabilize optimization. PocketGS achieves the best overall quality while remaining fast. Notably, 3DGS-MVS-WK performs poorly despite a larger Count, suggesting that a generic dense prior does not ensure good convergence in this regime. In contrast, PocketGS attains higher quality with fewer Gaussians, indicating better representation efficiency and conditioning under the same iteration budget.

Fig. 4 shows PocketGS better preserves fine, high-frequency geometry structures (e.g., *leaves in Fern*, *petals in Flower*), with fewer floating artifacts and cleaner boundaries. This is consistent with our refined geometry prior ($\mathcal{G}$) and robust anisotropic initialization ($\mathcal{I}$), which improve pose/structure consistency and reduce Gaussian drift during optimization.

b) NeRF-Synthetic Dataset.: On the geometry-clean NeRF Synthetic dataset, 3DGS-MVS-WK achieves the best metrics, as its dense prior matches the ground-truth geometry. PocketGS remains competitive (PSNR 24.32 vs. 24.47) while being $\sim 5.2\times$ faster in end-to-end runtime T_{total} (101.4s vs. 532.1s), mainly by avoiding the costly offline dense reconstruction in 3DGS-MVS-WK. With a similar Count (47k vs. 50k), this speedup reflects a more streamlined pipeline and hardware-aligned splatting rather than reduced capacity.

Fig. 5 shows PocketGS preserves high-fidelity appearance and clean edges under the same budget, closely matching 3DGS-MVS-WK, demonstrating that PocketGS can substantially reduce capture-to-reconstruction latency without sacrificing quality when geometry is well-conditioned.

c) MobileScan Dataset.: On the challenging MobileScan dataset, PocketGS consistently outperforms 3DGS-SFM-WK, indicating that our mobile-native prior construction mitigates instability from sparse/noisy mobile inputs. Compared to 3DGS-MVS-WK, PocketGS achieves better perceptual quality (LPIPS 0.225 vs. 0.281) with much lower end-to-end time (255.2s vs. 534.5s), suggesting that heavyweight offline dense reconstruction is inefficient for mobile deployment. Notably, although PocketGS and 3DGS-MVS-WK converge to similar primitives, PocketGS renders more faithfully, implying improved *placement* rather than merely the *quantity* of Gaussians.

Fig. 3 shows that 3DGS-SFM-WK often yields blurry textures and structural collapse, consistent with its low Count (23k) and unreliable geometry. While 3DGS-MVS-WK starts from a dense prior, it still exhibits artifacts when Gaussians are overly concentrated; under a limited optimization budget, it cannot sufficiently re-balance spatial coverage, leading to ghosting and local inconsistency. PocketGS avoids this by surface-aligned, spatially balanced anisotropic initialization,

Fig. 6: **Qualitative results on a mobile device across diverse datasets.** We showcase real-time rendering screenshots from an iPhone 15, covering our self-collected scenes (rows 1-2), LLFF (row 3), and NeRF Synthetic (row 4). PocketGS consistently achieves high-fidelity reconstruction and sharp details across varying scene scales and capture conditions. The red labels indicate optimized point counts, demonstrating our method's representation efficiency and robust generalization for practical on-device deployment.

producing sharper textures and higher structural fidelity closer to GT.

d) On-device Rendering and Deployment Perspective.: Beyond metrics, Fig. 6 demonstrates real-time rendering screenshots produced on an iPhone 15 across MobileScan, LLFF, and NeRF Synthetic scenes. The consistently sharp details across diverse scales and capture conditions indicate robust generalization in practical deployment. PocketGS maintains high perceptual quality under mobile memory and bandwidth constraints by avoiding unnecessary densification while preserving critical structures.

C. Memory Footprint

We profile peak memory usage on MobileScan to quantify the practicality of our on-device pipeline. Following our end-to-end definition, we report memory for two stages: (i) geometry prior construction and (ii) full 3DGS training. In all measurements, peak memory is recorded as the maximum resident memory observed during execution, and the statistics are aggregated over all MobileScan scenes.

Full 3DGS training reaches an average peak of 2.21 GB (range: 1.82–2.65 GB), reflecting the combined cost of storing the Gaussian parameters, intermediate buffers for rasterization, and optimizer states. Geometry prior construction peaks at 1.53 GB on average (range: 1.19–2.22 GB), dominated by temporary buffers used for feature processing, correspondence aggregation, and incremental updates of the prior representation. Importantly, across all scenes the peak memory remains below 3 GB, which fits within the on-device budget and leaves practical headroom for commodity smartphones to accommodate system overhead and concurrent background processes. We provide per-scene peak memory breakdowns for both stages in the supplemental material.

Variant	PSNR↑	SSIM↑	LPIPS↓	Time↓(s)
PocketGS (Full)	**23.67**	**0.791**	**0.225**	255.2
w/o Initialization ($\mathcal{I}$)	22.49	0.7696	0.253	319.5
w/o Global BA	23.45	0.7517	0.232	251.1
w/o MVS	21.07	0.6461	0.414	**124.8**

TABLE II: **Ablation Summary on MobileScan Dataset (Averages).**

D. Ablation Study

We conduct an ablation study on the MobileScan dataset to quantify the contribution of each core component of PocketGS. The study follows the same experiment setup, and we summarize dataset averages in Table II.

Information-Gated Frame Subsampling. Removing information-gated subsampling admits motion/defocus-

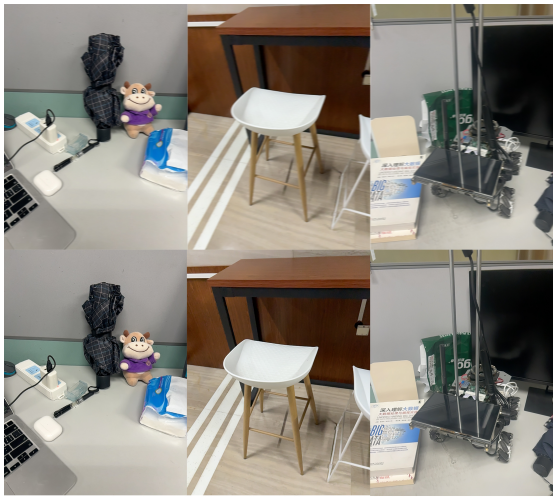

Fig. 7: Ablation of information-gated frame subsampling. Our method can obtain better details information.

degraded frames, corrupting the geometry prior and cascading into poorer initialization and blurrier reconstructions; the full pipeline better preserves sharp details (fig. 7).

GPU-native Global BA. Disabling Global BA yields a clear SSIM drop (from 0.791 to 0.7517) with minor PSNR/LPIPS changes, indicating reduced global coherence and pose consistency, while incurring negligible runtime overhead (251.1s vs. 255.2s).

Single-Reference Cost-Volume MVS. Removing lightweight MVS causes the largest quality degradation (PSNR 21.07, SSIM 0.6461, LPIPS 0.4137), showing dense geometric support largely sets the quality ceiling; although runtime drops to 124.8s, quality falls to the level of 3DGS-SFM-WK.

Prior-Conditioned Gaussian Parameterization. Removing $\mathcal{I}$ degrades all metrics (PSNR 23.67→22.49) and increases end-to-end time (255.2s→319.5s), suggesting prior-conditioned initialization is critical for convergence efficiency under a limited iteration budget.

V. Conclusion

We introduce PocketGS, a fully on-device 3DGS training paradigm that co-designs geometry priors ($\mathcal{G}$), prior-conditioned initialization ($\mathcal{I}$), and hardware-aligned splatting optimization ($\mathcal{T}$) to make high-fidelity 3D reconstruction practical under mobile compute and memory constraints. PocketGS achieves perceptual quality competitive with or superior to workstation baselines while meeting smartphone budgets (e.g., $\sim$4-minute end-to-end training and < 3 GB peak memory on iPhone 15), enabling practical professional-grade mobile 3D content creation for mixed reality and digital twins.

References

[1] B. Kerbl, G. Kopanas, T. Leimkühler, and G. Drettakis, "3d gaussian splatting for real-time radiance field rendering," *ACM Trans. Graph.*, vol. 42, no. 4, 2023.

[2] J. Gao, C. Gu, Y. Lin, Z. Li, H. Zhu, X. Cao, L. Zhang, and Y. Yao, "Relightable 3D Gaussians: Realistic Point Cloud Relighting with BRDF Decomposition and Ray Tracing," in *ECCV*, 2024.

[3] Z. Liang, Q. Zhang, Y. Feng, Y. Shan, and K. Jia, "GS-IR: 3D Gaussian Splatting for Inverse Rendering," in *CVPR*, 2024.

[4] B. Huang, Z. Yu, A. Chen, A. Geiger, and S. Gao, "2d gaussian splatting for geometrically accurate radiance fields," *ACM SIGGRAPH 2024 Conference Proceedings*, 2024.

[5] Z. Yu, T. Sattler, and A. Geiger, "Gaussian Opacity Fields: Efficient Adaptive Surface Reconstruction in Unbounded Scenes," *ACM TOG*, vol. 43, no. 6, pp. 1–13, 2024.

[6] A. Escontrela, J. Kerr, A. Allshire, J. Frey, R. Duan, C. Sferrazza, and P. Abbeel, "GaussGym: An Open-Source Real-to-Sim Framework for Learning Locomotion from Pixels," *arXiv preprint arXiv:2510.15352*, 2025.

[7] M. Zhang, K. Zhang, and Y. Li, "Dynamic 3D Gaussian Tracking for Graph-Based Neural Dynamics Modeling," in *CoRL*, 2025.

[8] B. Mildenhall, P. P. Srinivasan, M. Tancik, J. T. Barron, R. Ramamoorthi, and R. Ng, "Nerf: Representing scenes as neural radiance fields for view synthesis," *Communications of the ACM*, vol. 65, no. 1, pp. 99–106, 2021.

[9] A. Tewari, J. Thies, B. Mildenhall, P. Srinivasan, E. Tretschk, W. Yifan, C. Lassner, V. Sitzmann, R. Martin-Brualla, S. Lombardi *et al.*, "Advances in neural rendering," in *Computer Graphics Forum*, vol. 41, no. 2. Wiley Online Library, 2022, pp. 703–735.

[10] K. Gao, Y. Gao, H. He, D. Lu, L. Xu, and J. Li, "Nerf: Neural radiance field in 3d vision, a comprehensive review," *arXiv preprint arXiv:2210.00379*, 2022.

[11] J. T. Barron, B. Mildenhall, M. Tancik, P. Hedman, R. Martin-Brualla, and P. P. Srinivasan, "Mip-NeRF: A Multiscale Representation for Anti-Aliasing Neural Radiance Fields," in *ICCV*, 2021.

[12] J. T. Barron, B. Mildenhall, M. Tancik, P. P. Srinivasan, X. Han, and R. Martin-Brualla, "Mipnerf 360: Unbounded anti-aliased neural radiance fields," in *IEEE/CVF Conference on Computer Vision and Pattern Recognition (CVPR)*, 2022.

[13] S. Fridovich-Keil, A. Yu, M. Tancik, Q. Chen, B. Recht, and A. Kanazawa, "Plenoxels: Radiance fields without neural networks," in *Proceedings of the IEEE/CVF conference on computer vision and pattern recognition*, 2022, pp. 5501–5510.

[14] C. Sun, M. Sun, and H.-T. Chen, "Direct Voxel Grid Optimization: Super-Fast Convergence for Radiance Fields Reconstruction," in *CVPR*, 2022.

[15] T. Müller, A. Evans, C. Schied, and A. Keller, "Instant neural graphics primitives with a multiresolution hash encoding," *ACM Trans. Graph.*, vol. 41, no. 4, 2022.

[16] J. T. Barron, B. Mildenhall, D. Verbin, P. P. Srinivasan, and P. Hedman, "Zip-NeRF: Anti-Aliased Grid-Based Neural Radiance Fields," in *ICCV*, 2023.

[17] W. Guo, B. Wang, and L. Chen, "Neuv-slam: Fast neural multiresolution voxel optimization for rgbd dense slam," *IEEE Transactions on Multimedia*, 2025.

[18] G. Fang and B. Wang, "Mini-splatting: Representing scenes with a constrained number of gaussians," in *European Conference on Computer Vision*. Springer, 2024, pp. 165–181.

[19] ——, "Mini-splatting2: Building 360 scenes within minutes via aggressive gaussian densification," *arXiv preprint arXiv:2411.12788*, 2024.

[20] Z. Peng, T. Shao, Y. Liu, J. Zhou, Y. Yang, J. Wang, and K. Zhou, "Rtg-slam: Real-time 3d reconstruction at scale using gaussian splatting," *ACM SIGGRAPH 2024 Conference Proceedings*, 2024.

[21] C. Yan, D. Qu, D. Xu, B. Zhao, Z. Wang, D. Wang, and X. Li, "Gs-slam: Dense visual slam with 3d gaussian splatting," in *Proceedings of the IEEE/CVF Conference on Computer Vision and Pattern Recognition (CVPR)*, 2024.

[22] G. Wenzhi, B. Haiyang, M. Yuanqu, L. Jia, and C. Lijun, "Fvloc-nerf: Fast vision-only localization within neural radiation field," in *2023 IEEE/RSJ International Conference on Intelligent Robots and Systems (IROS)*. IEEE, 2023, pp. 3329–3334.

[23] D. Chen, H. Li, W. Ye, Y. Wang, W. Xie, S. Zhai, N. Wang, H. Liu, H. Bao, and G. Zhang, "PGSR: Planar-based Gaussian Splatting for Efficient and High-Fidelity Surface Reconstruction," *IEEE TVCG*, 2024.

[24] L. Höllein, A. Božič, M. Zollhöfer, and M. Nießner, "3dgs-lm: Faster gaussian-splatting optimization with levenberg-marquardt," in *Proceedings of the IEEE/CVF International Conference on Computer Vision*, 2025, pp. 26 740–26 750.

[25] Y. Chen, J. Jiang, K. Jiang, X. Tang, Z. Li, X. Liu, and Y. Nie, "Dashgaussian: Optimizing 3d gaussian splatting in 200 seconds," in *Proceedings of the Computer Vision and Pattern Recognition Conference*, 2025, pp. 11 146–11 155.

[26] G. Fang and B. Wang, "Efficient Scene Modeling Via Structure-Aware and Region-Prioritized 3D Gaussians," *IEEE TPAMI*, 2025.

[27] B. Triggs, P. F. McLauchlan, R. I. Hartley, and A. W. Fitzgibbon, "Bundle adjustment — a modern synthesis," in *Vision Algorithms: Theory and Practice*. Springer, 1999.
[28] J. L. Schönberger and J.-M. Frahm, "Structure-from-motion revisited," in *Proceedings of the IEEE Conference on Computer Vision and Pattern Recognition (CVPR)*, 2016.
[29] Q. Picard, S. Chevobbe, M. Darouich, and J.-Y. Didier, "A survey on real-time 3d scene reconstruction with slam methods in embedded systems," *arXiv preprint arXiv:2309.05349*, 2023.
[30] T. Qin, P. Li, and S. Shen, "Vins-mono: A robust and versatile monocular visual-inertial state estimator," *IEEE Transactions on Robotics*, vol. 34, no. 4, pp. 1004–1020, 2018.
[31] Y. Furukawa and J. Ponce, "Accurate, dense, and robust multiview stereopsis," *IEEE transactions on pattern analysis and machine intelligence*, vol. 32, no. 8, pp. 1362–1376, 2009.
[32] Y. Yao, Z. Luo, S. Li, T. Fang, and L. Quan, "Mvsnet: Depth inference for unstructured multi-view stereo," in *European Conference on Computer Vision (ECCV)*, 2018.
[33] P. Kim, J. Kim, M. Song, Y. Lee, M. Jung, and H.-G. Kim, "A benchmark comparison of four off-the-shelf proprietary visual–inertial odometry systems," *Sensors*, vol. 22, no. 24, p. 9873, 2022.
[34] T. Feigl, A. Porada, S. Steiner, C. Löffler, C. Mutschler, and M. Philippsen, "Localization limitations of arcore, arkit, and hololens in dynamic large-scale industry environments." in *VISIGRAPP (1: GRAPP)*, 2020, pp. 307–318.
[35] R. Mur-Artal and J. D. Tardós, "Orb-slam2: An open-source slam system for monocular, stereo, and rgb-d cameras," *IEEE transactions on robotics*, vol. 33, no. 5, pp. 1255–1262, 2017.
[36] Z. Chen, T. Funkhouser, P. Hedman, and A. Tagliasacchi, "Mobilenerf: Exploiting the polygon rasterization pipeline for efficient neural field rendering on mobile architectures," in *Proceedings of the IEEE/CVF Conference on Computer Vision and Pattern Recognition*, 2023, pp. 16 569–16 578.
[37] S. Rojas, J. Zarzar, J. C. Pérez, J. Sanchez-Riera, A. Rodríguez, F. Segu, and F. Moreno-Noguer, "Re-rend: Real-time rendering of nerfs across devices," in *Proceedings of the IEEE/CVF International Conference on Computer Vision (ICCV)*, 2023.
[38] W. S. Fife and J. K. Archibald, "Improved census transforms for resource-optimized stereo vision," *IEEE Transactions on Circuits and Systems for Video Technology*, vol. 23, no. 1, pp. 60–73, 2012.
[39] X. Yang, L. Zhou, H. Jiang, Z. Tang, Y. Wang, H. Bao, and G. Zhang, "Mobile3drecon: Real-time monocular 3d reconstruction on a mobile phone," *IEEE Transactions on Visualization and Computer Graphics*, vol. 26, no. 12, pp. 3446–3456, 2020.
[40] B. Mildenhall, P. P. Srinivasan, R. Ortiz-Cayon, N. K. Kalantari, R. Ramamoorthi, R. Ng, and A. Kar, "Local light field fusion: Practical view synthesis with prescriptive sampling guidelines," *ACM Transactions on Graphics (ToG)*, vol. 38, no. 4, pp. 1–14, 2019.

APPENDIX

In this section, we provide additional details regarding the three core operators of PocketGS: Geometry Prior Construction ($\mathcal{G}$), Prior-Conditioned Parameterization ($\mathcal{I}$), and Hardware-Aligned Splatting ($\mathcal{T}$).

A. Geometry Prior Construction ($\mathcal{G}$)

a) Information-Gated Frame Selection: To ensure high-quality input under a limited time budget, we implement a real-time frame selection mechanism during the capture phase. We utilize a displacement gate $\tau = 0.05$m to filter redundant frames. For frames passing the displacement gate, we employ a candidate window mechanism (maximum 8 frames or 0.25s) to select the sharpest frame. Sharpness is computed by calculating the gradient energy on a sparse 160×160 grid of the luma plane, prioritizing frames with higher high-frequency content to mitigate motion blur.

b) GPU-Native Global Bundle Adjustment: Our global BA optimizes both camera poses and 3D point coordinates. We establish geometric constraints by extracting ORB/FAST features with BRIEF descriptors, accelerated via Metal. Feature matching is performed using Hamming distance with ratio tests and cross-checks. We implement an iterative refinement process (typically 3 rounds) that includes re-triangulation and outlier filtering based on reprojection error and triangulation angles. The optimization uses a Levenberg-Marquardt (LM) solver with Schur complement, fully resident on the GPU. To fix the gauge, we anchor the first frame's 6DoF and the scale of the baseline between the first two frames.

c) Lightweight Single-Reference MVS: For dense reconstruction, we estimate per-frame depth maps using a plane-sweep algorithm. To optimize memory, we select the top-3 reference frames based on baseline distance and viewing angle but only utilize the best reference frame for cost volume construction. The depth search range is dynamically estimated using the 5%–95% quantiles of sparse point depths. We use Census transform for robust matching and Semi-Global Matching (SGM) for cost aggregation. The final dense point cloud is generated by back-projecting pixels with confidence ≥ 0.4 and depth within 0.05m to 5.0m.

B. Prior-Conditioned Parameterization ($\mathcal{I}$)

We initialize Gaussian primitives by leveraging the local surface statistics derived from the MVS point cloud. For each point, we estimate the local surface normal using PCA on its $k = 16$ nearest neighbors. The scale parameters are initialized based on the average distance to the $k = 3$ nearest neighbors. To seed anisotropic Gaussians, we set the scale along the normal direction to $0.3\times$ the tangential scales, effectively creating disc-like primitives that better align with the scene geometry.

C. Hardware-Aligned Splatting ($\mathcal{T}$)

Our differentiable renderer is tailored for Tile-Based Deferred Rendering (TBDR) GPUs. We implement a multi-stage pipeline where alpha compositing is manually unrolled within the fragment shader. This allows us to cache intermediate states in tile memory, avoiding expensive global memory traffic. For backpropagation, we use index-mapped gradient scattering to ensure that gradients are correctly accumulated into the canonical parameter buffer despite the depth-sorted rendering order.

To demonstrate the feasibility and practicality of our end-to-end on-device training system, we developed a dedicated mobile application, PocketGS, which integrates the entire pipeline from data capture to 3DGS training. The application is built on the Metal framework for high-performance GPU computation.

The application workflow, as illustrated in Figure 8, is designed to be intuitive and efficient:

- **Main Menu (Fig. 8a):** Provides access to the core functionalities: Splat Capture (data acquisition), View

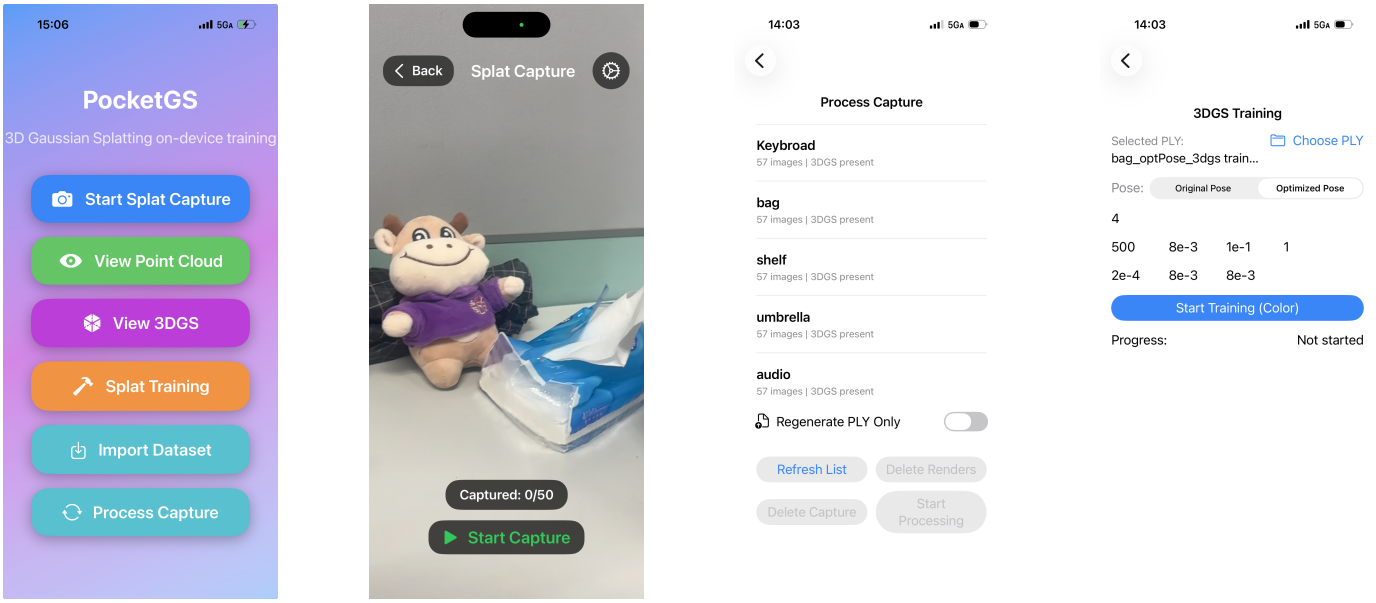

(a) Main Menu (b) Splat Capture (c) Process Capture (d) Splat Training

Fig. 8: Screenshots of the PocketGS mobile application, illustrating the end-to-end workflow.

Point Cloud and View 3DGS (visualization), Splat Training (optimization), Import Dataset, and Process Capture (geometry prior construction).

- **Splat Capture (Fig. 8b):** A guided capture interface that uses the information-gated frame selection mechanism to ensure high-quality input images (e.g., 50 frames) are collected in real-time, minimizing motion blur and redundancy.
- **Process Capture (Fig. 8c):** This module manages captured scenes and executes the Geometry Prior Construction ($\mathcal{G}$) operator, including the GPU-native BA and lightweight MVS, to generate the initial PLY point cloud. Users can manage captured data and trigger the processing step.
- **Splat Training (Fig. 8d):** This interface allows users to configure and initiate the on-device 3DGS training. Key features include selecting the input PLY file, choosing between Original Pose (ARKit pose) and Optimized Pose (BA-refined pose), and setting core hyperparameters (e.g., learning rates, iterations). The training process, which implements the $\mathcal{I}$ and $\mathcal{T}$ operators, runs entirely on the mobile GPU, with progress displayed in real-time.

The PocketGS app serves as a concrete proof-of-concept, demonstrating that high-quality 3DGS training can be achieved end-to-end on a commodity mobile device within minutes.

The MobileScan dataset consists of 16 diverse indoor and outdoor scenes captured using iPhone 15. The statistics of the collected scenes are summarized in Table III. Each scene includes 50 high-resolution images with corresponding ARKit poses and sparse point clouds as baselines, as shown on 9.

The dataset covers various challenging scenarios, including:

- **Textureless Surfaces:** Large uniform areas like the ”Sofa” and ”Desk” scenes.
- **Complex Geometry:** Intricate structures in the ”Transformer” and ”Shrub” scenes.
- **Varying Lighting:** Outdoor scenes like ”Pier” with natural lighting transitions.

Fig. 9: The scenes on MobileScan Dataset.

Category	Scenes	Environment
Furniture	Sofa,Table, Desk, Shelf	Indoor
Objects	Robot, Audio, Printer, Bag, Elxbox, audio.	Indoor
Outdoor	Pier, Shrub, Bench, Bike, Transformer, Chair, Flowerpot	Outdoor

TABLE III: Statistics of the MobileScan Dataset.

We provide per-scene metrics for our MobileScan dataset, NeRF Synthetic dataset, and LLFF dataset. These tables serve as the full, unaggregated data supporting the main paper's claims on performance metrics (PSNR, SSIM, LPIPS) and efficiency (Time, Count).

Scene	3DGS-SFM-WK					3DGS-MVS-WK					PocketGS (Ours)				
	PSNR ↑	SSIM ↑	LPIPS ↓	Time (s) ↓	Count	PSNR ↑	SSIM ↑	LPIPS ↓	Time (s) ↓	Count	PSNR ↑	SSIM ↑	LPIPS ↓	Time (s) ↓	Count
Pier	20.23	0.498	0.495	**156.0**	35800	**20.54**	**0.695**	**0.312**	519.6	200936	20.29	0.625	0.329	212.8	176804
Chair	22.13	0.542	0.421	**174.0**	39420	21.34	**0.699**	0.270	555.1	180664	**22.39**	0.670	**0.256**	240.7	176970
Flowerpot	20.93	0.595	0.424	**168.0**	32415	21.00	**0.730**	0.281	486.9	242616	**21.97**	0.725	**0.225**	265.7	241976
Shrub	18.88	0.507	0.481	**204.0**	37476	18.53	0.582	0.427	546.7	98616	**18.94**	**0.609**	**0.331**	230.0	174278
Transformer	20.49	0.542	0.465	**162.0**	27678	19.66	**0.636**	0.360	546.7	122117	**21.05**	0.636	**0.315**	209.7	126222
Sofa	14.26	0.611	0.558	**28.6**	38	**25.32**	0.870	0.222	525.4	312949	24.90	**0.873**	**0.192**	389.4	289848
Table	19.71	0.754	0.382	**78.0**	18873	15.01	0.727	0.365	401.9	113738	**22.85**	**0.852**	**0.194**	184.6	179940
Robot	22.90	0.807	0.285	**114.0**	20795	22.21	**0.862**	0.207	581.7	209226	**24.64**	0.850	**0.167**	291.9	194881
Desk	20.31	0.754	0.313	**72.0**	20735	17.42	0.750	0.279	491.9	111202	**22.03**	**0.838**	**0.172**	192.8	108018
Elebox	26.17	0.922	0.197	**22.4**	4410	21.11	0.899	0.181	575.8	52654	**27.75**	**0.936**	**0.136**	255.1	37182
audio	26.05	0.815	0.330	**150.0**	28628	23.97	0.852	0.263	520.0	147733	**27.69**	**0.857**	**0.166**	270.2	155278
bag	23.71	0.855	0.313	**108.0**	22584	21.35	0.865	0.260	533.0	170320	**24.79**	0.859	**0.210**	320.4	179101
fireExtin	23.94	0.879	0.274	**96.0**	18162	22.09	0.886	0.239	592.0	146224	**26.40**	**0.896**	**0.170**	279.8	123325
printer	22.56	0.804	0.376	**59.8**	10368	20.08	0.834	0.277	542.8	203770	**26.30**	**0.882**	**0.202**	282.6	196896
shelf	20.39	0.761	0.418	**24.8**	4860	21.17	0.811	0.313	518.8	77940	**25.40**	**0.872**	**0.226**	224.4	75872
umbrella	**24.29**	0.813	0.341	**47.4**	9736	21.98	0.845	0.273	581.8	179388	23.30	0.826	**0.235**	261.9	173587
Average	21.16	0.687	0.398	**112.8**	23486	20.85	0.781	0.281	534.5	165367	**23.67**	**0.791**	**0.225**	255.2	168009

TABLE IV: **MobileScan dataset comparison.** Best results are highlighted in **bold**

Scene	3DGS-SFM-WK					3DGS-MVS-WK					PocketGS (Ours)				
	PSNR↑	SSIM↑	LPIPS↓	Time (s)↓	Count	PSNR↑	SSIM↑	LPIPS↓	Time (s)↓	Count	PSNR↑	SSIM↑	LPIPS↓	Time (s)↓	Count
Chair	22.11	0.869	0.154	90.0	14433	**25.37**	**0.957**	**0.054**	692.4	60859	23.70	0.870	0.089	**85.7**	49857
Drums	18.78	0.762	0.268	**53.8**	12842	**21.27**	**0.861**	**0.154**	570.1	60640	20.97	0.775	0.183	130.1	58511
Ficus	19.99	0.812	0.212	44.2	1511	20.36	0.804	0.233	144.3	5674	**22.94**	**0.879**	**0.134**	**33.5**	5638
Hotdog	23.13	0.829	0.236	84.0	9703	**29.09**	**0.966**	**0.050**	571.3	40686	28.07	0.940	0.094	**78.8**	38583
Lego	22.02	0.795	0.228	132.0	29883	**25.47**	**0.930**	**0.092**	770.3	73821	24.92	0.872	0.124	**130.5**	74572
Materials	21.21	0.779	0.254	120.0	6934	22.45	**0.843**	0.170	414.8	51456	**22.85**	0.842	**0.158**	**117.4**	52137
Mic	23.62	0.859	0.205	**31.7**	5879	**27.11**	**0.936**	**0.066**	519.5	39553	26.24	0.901	0.120	81.0	36082
Ship	23.14	0.696	0.386	**114.0**	15006	24.60	**0.798**	**0.202**	574.5	69482	**24.87**	0.781	0.248	153.9	64208
Average	21.75	0.800	0.243	**83.7**	12024	**24.47**	**0.887**	**0.128**	532.1	50271	24.32	0.858	0.144	101.4	47449

TABLE V: NeRF Synthetic Dataset comparison.

D. MobileScan Dataset Comparison

The detailed per-scene quantitative results on our d MobileScan dataset are presented in Table IV. PocketGS consistently outperforms 3DGS-SFM-WK and 3DGS-MVS-WK in terms of perceptual quality (LPIPS) while maintaining a significantly lower training time than the dense baseline.

E. NeRF Synthetic and LLFF Datasets

We also evaluate PocketGS on standard benchmarks to demonstrate its generalization capability. The per-scene results for the NeRF Synthetic dataset are shown in Table V, and the LLFF dataset results are in Table VI.

We analyze the peak memory usage of PocketGS during the MVS and training phases. The detailed per-scene memory usage is provided in Table VII, demonstrating that our system operates well within the memory budget of commodity mobile devices.

We conduct ablation studies to evaluate the impact of our core components. The following tables provide the detailed per-scene metrics for each ablation configuration, serving as the full data to support the aggregated results presented in the main paper.

F. Ablation: w/o Initialization ($\mathcal{I}$)

This configuration removes the prior-conditioned anisotropic seeding in $\mathcal{I}$, reverting to isotropic initialization. The detailed per-scene results in Table VIII show a significant drop in performance, highlighting the importance of geometry-aware initialization for fast convergence.

G. Ablation: w/o Global BA

This configuration removes the GPU-native global Bundle Adjustment (BA) in $\mathcal{G}$, relying solely on the initial ARKit poses. The detailed per-scene results in Table IX indicate that the global BA is crucial for refining the coarse mobile poses, leading to better reconstruction quality.

H. Ablation: w/o MVS

This configuration removes the lightweight single-reference MVS in $\mathcal{G}$, relying only on the sparse point cloud from ARKit for initialization. The significant drop in all metrics, as shown in Table X, demonstrates the necessity of a dense, geometry-faithful prior for achieving high perceptual quality within a limited training budget.

Scene	3DGS-SFM-WK					3DGS-MVS-WK					PocketGS (Ours)				
	PSNR↑	SSIM↑	LPIPS↓	Time↓(s)	Count	PSNR↑	SSIM↑	LPIPS↓	Time↓(s)	Count	PSNR↑	SSIM↑	LPIPS↓	Time↓(s)	Count
Fern	21.11	0.649	0.415	**21.0**	11436	21.36	0.707	0.335	118.2	38816	**25.75**	**0.849**	**0.182**	107.4	29220
Flower	22.97	0.701	0.328	114.0	22440	20.53	0.632	0.381	316.4	34914	**25.06**	**0.818**	**0.187**	**92.0**	28523
Fortress	26.51	0.744	0.321	180.0	29365	23.59	0.762	0.277	551.9	69762	**27.15**	**0.901**	**0.129**	**91.6**	67120
Horns	21.19	0.674	0.412	**126.0**	22335	17.42	0.626	0.432	530.9	38403	**23.39**	**0.806**	**0.233**	148.6	35996
Leaves	15.36	0.352	0.600	246.0	9358	15.28	0.327	0.588	190.4	20315	**15.77**	**0.456**	**0.501**	**60.8**	9358
Orchids	18.85	0.562	0.401	**66.0**	21968	18.11	0.593	0.353	141.1	66975	**21.73**	**0.772**	**0.183**	138.9	55320
Room	21.70	0.764	0.400	**15.3**	4737	21.34	0.787	0.358	203.4	27610	**26.18**	**0.897**	**0.168**	75.6	19273
Trex	20.42	0.684	0.360	**96.0**	21645	18.62	0.664	0.376	452.4	30104	**23.33**	**0.830**	**0.194**	128.6	22349
Average	21.01	0.641	0.405	108.0	17910	19.53	0.637	0.387	313.1	40862	**23.54**	**0.791**	**0.222**	**105.4**	33395

TABLE VI: **LLFF dataset comparison.**

Metric	audio	printer	fireExtin	flowerpot	Elebox	desk	transformer	shrub	bench	sofa	Keybroad	bike	Pier	bag	robot	umbrella	chair	table	shelf	Avg.
MVS Peak Mem. (GB)	1.55	1.50	1.55	1.48	1.38	1.19	1.48	1.64	2.22	1.39	1.67	1.50	1.73	1.42	1.57	1.56	1.49	1.24	1.47	1.53
Training Peak Mem. (GB)	2.65	2.62	2.50	2.49	2.44	2.41	2.29	2.27	2.20	2.15	2.15	2.12	2.03	2.02	1.98	1.95	1.94	1.91	1.82	2.21

TABLE VII: Per-scene peak memory.

Metric	Elebox	Pier	audio	bag	bench	bike	chair	desk	fireExtin	flowerpot	printer	robot	shelf	shrub	sofa	table	transformer	umbrella	**Avg.**
PSNR (dB)	27.03	20.16	20.93	22.72	21.97	23.02	22.09	22.07	26.46	20.98	24.83	21.35	24.99	18.80	22.05	22.89	20.91	21.55	**22.49**
SSIM	0.9335	0.6048	0.8138	0.8303	0.6859	0.7185	0.6514	0.8385	0.8961	0.6836	0.8555	0.7934	0.8647	0.5889	0.8203	0.8522	0.6255	0.7955	**0.7696**
LPIPS	0.1400	0.3572	0.1859	0.2628	0.3207	0.2553	0.2760	0.1726	0.1781	0.2735	0.2390	0.2259	0.2481	0.3588	0.2706	0.1935	0.3316	0.2699	**0.2533**
Time (s)	369.1	325.6	363.0	335.8	350.4	327.7	306.8	186.7	429.2	386.9	352.7	283.0	318.3	331.5	329.3	172.6	297.7	284.5	**319.5**

TABLE VIII: Per-scene metrics **w/o initialization** (removing prior-conditioned anisotropic seeding in $\mathcal{I}$).

Metric	Elebox	Pier	audio	bag	bench	bike	chair	desk	fireExtin	flowerpot	printer	robot	shelf	shrub	sofa	table	transformer	umbrella	**Avg.**
PSNR (dB)	27.61	20.21	26.95	24.47	22.40	23.03	22.30	22.02	26.45	21.67	26.10	24.38	24.85	18.82	24.49	22.52	20.80	23.01	**23.45**
SSIM	0.8975	0.5910	0.8156	0.8201	0.6869	0.6832	0.6318	0.8014	0.8548	0.6843	0.8401	0.8048	0.8282	0.5774	0.8283	0.8107	0.5915	0.7825	**0.7517**
LPIPS	0.1350	0.3253	0.1743	0.2172	0.2857	0.2595	0.2639	0.1758	0.1821	0.2326	0.2093	0.1869	0.2367	0.3311	0.1928	0.2026	0.3285	0.2437	**0.2324**
Time (s)	230.7	212.2	280.5	311.5	259.9	231.9	233.5	181.3	285.0	254.2	282.5	263.2	232.0	230.6	352.7	176.7	238.5	263.0	**251.1**

TABLE IX: Per-scene metrics **w/o global BA** (removing GPU-native global BA in $\mathcal{G}$).

Metric	Elebox	Pier	audio	bag	bench	bike	chair	desk	fireExtin	flowerpot	printer	robot	shelf	shrub	sofa	table	transformer	umbrella	**Avg.**
PSNR (dB)	23.10	18.25	24.43	23.67	19.84	21.03	19.46	20.12	23.35	19.56	23.38	22.66	21.09	16.98	21.96	19.61	18.91	21.92	**21.07**
SSIM	0.9029	0.3181	0.7425	0.8163	0.4339	0.5333	0.3467	0.7574	0.8413	0.5089	0.8195	0.7925	0.7845	0.2820	0.7690	0.7533	0.4489	0.7795	**0.6461**
LPIPS	0.2113	0.6392	0.3905	0.3201	0.5653	0.4897	0.5609	0.2855	0.3064	0.4894	0.3259	0.2600	0.3583	0.6229	0.3898	0.3478	0.5480	0.3366	**0.4137**
Time (s)	122.2	93.8	186.7	142.1	101.4	110.7	129.0	95.9	178.5	118.9	149.3	112.2	142.3	88.2	136.2	89.9	111.0	137.5	**124.8**

TABLE X: Per-scene metrics **w/o MVS** (removing lightweight single-reference MVS in $\mathcal{G}$).